TASK QUARTERLY vol. 18, No 1, 2014, pp. 81–100

VALIDATING FULL CAVITATION MODEL WITH AN EXPERIMENTAL CENTRIFUGAL PUMP

WEN-GUANG LI

Department of Fluid Machinery, Lanzhou University of Technology
730050 Lanzhou, Gansu, China
e-mail: Liwg43@163.com

(Received 30 January 2014; revised manuscript received 22 February 2014)

Abstract: The full cavitation model is increasingly applied in the cavitating flow simulation and the cavitation performance prediction of a centrifugal pump to improve or optimize its hydraulic design. Since the model involves surface tension and non-condensable gas content, it can be potentially applied in predicting cavitation behaviour of a centrifugal pump when handling viscous oils that possess different surface tension and gas content than water. However, the model has not been validated extensively against experimental incipient cavitation and NPSHr (net positive suction head required) data so far. In the paper, the cavitation performance of an experimental centrifugal pump is investigated using the CFD code and the full cavitation model when pumping water. The incipient cavitation number-flow rate curve and head-NPSHa (net positive suction head available) relationship are established and compared with experimental observations. The relationship between the head and integrated vapour-liquid volume ratio in the impeller is argued. The influence of the non-condensable gas content and turbulence model on the head-NPSHa curve is clarified. The cavity pattern predicted is compared with the visualized one. The computational methods adopted and the results achieved here can be useful for the cavitation performance prediction of a centrifugal pump in engineering.

Keywords: centrifugal pump, cavitation, incipient cavitation, suction performance, net positive suction head required, net positive suction head available, CFD

1. Introduction

The cavitation performance of a centrifugal pump is usually obtained experimentally, like the investigations in [1–6]. Recently, however, such performance has been tended to be estimated by employing a three-dimensional flow solver with a proper cavitation model, such as those studied in [7–25]. Furthermore, four kinds of cavitation models, namely Zwart-Gerber-Belamri [26], Schnerr-Sauer [27], Kunz [28] and the full caviation models [29] have been implanted in popular CFD codes such as ANSYS CFX, FLUENT, FINE TURBO and open access code-openFOAM.

Compared with the other two phase flow cavitation models in [26–28], the full cavitation model involves the liquid surface tension and non-condensable gas which can be important for the viscous oil cavitating flows. Obviously it has a potential for being applied in simulating a cavitating flow of liquid more than water, for instance viscous oils [30]. Unfortunately, this model has not been extensively validated against experimental incipient cavitation and NPSHr (net positive suction head required) data in centrifugal pumps so far [23].

On the one hand, viscous oil cavitating flows in a centrifugal pump have been attacked primarily by using the full cavitation model in [31] and its cavitation performance has been established, as well. In addition, the estimated correction factor for NPSHr against the impeller Reynolds number seems to agree well with the existing empirical correlation. However, this work is subject to a limitation that the cavitation model has not been validated with the existing experimental results even for water. As a result, it is unknown how large the difference between the CFD prediction and the observation in NPSHr is.

On the other hand, the incipient cavitation behaviour of a centrifugal pump can be predicted by using the single phase potential flow model [32, 33], the single phase viscid flow model [23] and the two phase cavitation model [19, 20, 23, 34]. The argument among them needs to be clarified. In the paper, the caviating flows of water in an experimental centrifugal pump used in [5, 6] are simulated by making use of FLUENT6.2 with the full cavitation model under various working conditions. The incipient cavitation number-flow rate curves and head-NPSHa (net positive suction head available) relationships are obtained and validated with the corresponding observations and measurements. The predicted NPSHr and blade cavitation coefficient were compared with the experimental results. At the design condition, the cavity aspects predicted by CFD are validated with the visualized cavity patterns.

The contributions to the subject include: (1) a hybrid mesh of tetrahedron with a core hexahedral cell, the staggered pressure interpolation scheme and the adaptive mesh technique are adopted in numerical computations; (2) the relationship between the pump head and the integrated vapour-liquid volume ratio is clarified and the effects of non-condensable gas content and turbulence model on head-NPSHa curve are explored; (3) the effects of the non-condensable gas content and turbulence model on NPSHr are identified.

2. Computational Models

The physical model of CFD is a one-stage, end-suction, cantilevered experimental centrifugal pump for cavitation visualization and NPSHr measurement in [5, 6]. The pump design flow rate Q, head H, rotational speed n and specific speed n_s are 210 m^3/h, 40 m and 2160 r/min, 116 ($n_s = 3.65n\sqrt{Q}/H^{3/4}$, r/min, m^3/s, m), respectively. The eye diameter, blade leading and trailing edges diameters are 100 mm, 130 mm and 278 mm. The blade entrance and discharge angles are 19° and 23°. There are five blades, and the blade metal is 6.5 mm thick and

23 mm wide. The blade is two-dimensional, and its camber line is composed of two segments of arc with the radius of 84 mm and 135 mm. A vaneless diffuser with constant width of 28 mm is located behind the impeller. Water is discharged into an annular collector from the diffuser. There are 12 axially orientated discharge pipes to lead water out of the pump. The axial cross-sectional drawing of the experimental pump is illustrated in Figure 1 (a) and a three-dimensional blade without shroud is exhibited in Figure 1 (b).

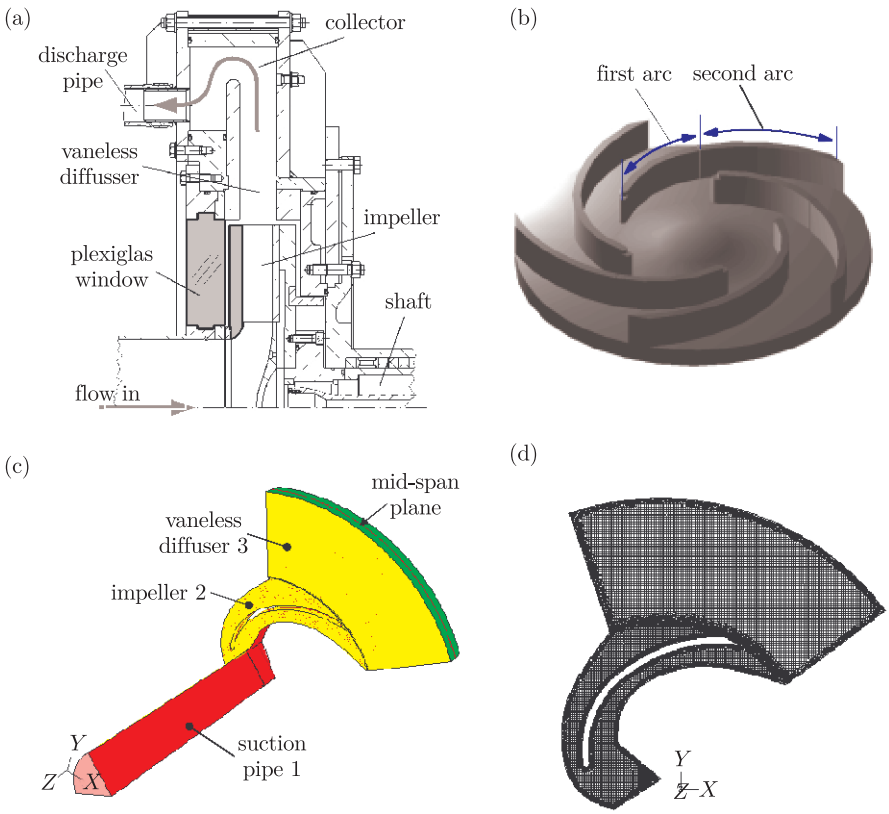

Figure 1. Geometrical model, blade shape, fluid domain and mesh pattern in mid-span plane of experimental centrifugal pump, (a) axial cross-section drawing [5, 6], (b) blade shape [5, 6], (c) fluid domains, (d) mesh pattern

The computational fluid domains consist of stationary suction pipe 1, rotating impeller 2 and stationary vaneless diffuser 3, see Figure 1 (c). There is a grid interface established on the boundary between the suction pipe and the impeller, and the same kind of interface is generated on that between the impeller and the diffuser, too. The MRF (multiple reference frame) method is used to handle the impeller rotating effect. Due to the rotational symmetry of the fluid domains, it is only the flow in one channel of the impeller that needs to be analysed.

The fluid domains and their mesh are built and created in GAMBIT. Hexahedral mesh is generated in the section pipe fluid domain, the impeller and vaneless diffuser fluid domains are discretized with mixed cells (tetrahedral cells near the domain boundaries, cubes in the rest area) in order to achieve a stable computational process.

Table 1. Number of cells in mesh in fluid domains

Mesh type	Change in mesh	Suction pipe	Impeller	Diffuser
mesh1	Initial mesh	28125	181567	276407
	Adaptive mesh	N/A	334790	289147
mesh2	Initial mesh	28125	258469	276407
	Adaptive mesh	N/A	367907	289393
mesh3	Initial mesh	28125	485999	330434
	Adaptive mesh	N/A	547809	336160

The mesh in the blade mid-span plane is presented in Figure 1 (d), and the numbers of cells in the fluid domains are shown in Table 1. In that table, the initial numbers of mesh cells and those adapted to satisfy the condition where y^+ $(= yu^*/\nu_l$, y is the shortest distance from a mesh node to a solid wall, u^* is the fluid shear or friction velocity, $u^* = \sqrt{\tau_w/\rho_l}$, τ_w is the shear stress on the wall applied by fluid, ρ_l is the fluid density at pumped temperature and ν_l is the kinematic viscosity of fluid) was in the range of 30–300, as proposed in [35]. The non-equilibrium wall function was applied to involve shear stress on the walls in the pump so as to account for the effect of the pressure gradient in the primary flow direction on the wall shear stress given in [36] as follows:

$$\begin{cases} \dfrac{\tilde{U} C_\mu^{1/4} k^{1/2}}{\tau_w/\rho_l} = \dfrac{1}{\kappa} \ln\left(E \dfrac{\rho_l C_\mu^{1/4} k^{1/2} y}{\mu_l} \right) \\ \tilde{U} = U - \dfrac{1}{2} \dfrac{dp}{dL} \left[\dfrac{y_v}{\rho_l \kappa \sqrt{k}} \ln\left(\dfrac{y}{y_v} \right) + \dfrac{y - y_v}{\rho_l \kappa \sqrt{k}} + \dfrac{y_v^2}{\mu_l} \right] \end{cases} \tag{1}$$

where U is the fluid velocity in the primary flow direction, μ_l is viscosity of fluid, κ, C_μ and E are the turbulence constants, y_v is the physical viscous sub-layer thickness and k is the kinetic energy of turbulence, p is the static pressure of fluid, and dp/dL is the pressure gradient in the primary flow direction. Clearly, the effect of dp/dL on the wall shear stress τ_w is involved in (1).

The working fluid during the experiment is water and it remains so in the CFD computation. Its viscosity, density and surface tension as well as its vapour density and viscosity are listed in Table 2 at 20°C. At this temperature, the concentration of non-condensable gas is 2 %–3 % (around 15 ppm) in [30] and this value is adopted in the CFD computation here.

In the pump, there is a flow of the mixture of water, its vapour and non-condensable gas, which is steady, three-dimensional, turbulent and isothermal. The flow governing equations include the continuity equation, Reynolds time-averaged N-S equations and vapour transport equation. Besides, the standard

Table 2. Physical parameters of pumped liquid and its vapour at 20°C

State	Density ρ_l, ρ_v (kg/m^3)	Kinematic viscosity ν_l, ν_v (mm^2/s)	Dynamic viscosity μ_l, μ_v (Pa·s)	Saturated vapour pressure p_{sat} (Pa)	Surface tension σ (N/m)	Non-condensable gas concentration α_g (ppm)
Liquid	998.2	1.0087	$1.0069\cdot10^{-3}$	2367.8	$7.17\cdot10^{-2}$	15
Vapour	0.5542	$2.4179\cdot10^{-2}$	$1.3400\cdot10^{-5}$			

two-equation turbulence model k-ε is launched to account for turbulent shear stresses. Those governing equations can be found in [36]. The continuity equation for the mixture is

$$\frac{\partial\rho}{\partial t}+\nabla\cdot(\rho\vec{v})=0 \tag{2}$$

where $\vec{v}$ is the mixture mass-averaged velocity, $\vec{v}=\sum_{i=l,v,g}\alpha_i\vec{v}_i/\rho$, α_i is the volume fraction of phase i, $i=l,v,g$, here l, v and g represent liquid, vapour and non-condensable gas phases, $\vec{v}_l$, $\vec{v}_v$ and $\vec{v}_g$ are the velocity of liquid, vapour and non-condensable gas, note that $\vec{v}_l=\vec{v}_v=\vec{v}_g$; ρ is the mixture density, $\rho=\alpha_v\rho_v+\alpha_g\rho_g+(1-\alpha_v-\alpha_g)\rho_l$, α_v and α_g represent the volume fractions of the vapour and non-condensable gas, respectively; the sum $\alpha_v+\alpha_g$ is the void fraction or porosity α; ρ_v and ρ_g are the vapour and non-condensable gas density.

The momentum equations of the mixture are the summary of liquid, vapour and non-condensable gas momentum equations. They can be expressed as

$$\frac{\partial}{\partial t}(\rho\vec{v})+\nabla\cdot(\rho\vec{v}\vec{v})=-\nabla p+\nabla\cdot\left[\mu(\nabla\vec{v}+\nabla\vec{v}^T)\right] \tag{3}$$

where μ is the dynamic viscosity of the mixture, $\mu=\alpha_l\mu_l+\alpha_v\mu_v+\alpha_g\mu_g$, μ_l, μ_v and μ_g are the dynamic viscosity of liquid, vapour and non-condensable gas.

For cavitating flows, the mixture turbulence model is the default multiphase turbulence model in FLUENT6.2. The mixture turbulence model is an extension of single-phase standard k-ε turbulence model. The k and ε equations in this model are as follows:

$$\frac{\partial}{\partial t}(\rho k)+\nabla\cdot(\rho\vec{v}k)=-\nabla\left(\frac{\mu_t}{\sigma_k}\nabla k\right)+G_k+\rho\varepsilon \tag{4}$$

and

$$\frac{\partial}{\partial t}(\rho\varepsilon)+\nabla\cdot(\rho\vec{v}\varepsilon)=-\nabla\left(\frac{\mu_t}{\sigma_\varepsilon}\nabla\varepsilon\right)+\frac{\varepsilon}{k}(C_{1\varepsilon}G_k-C_{2\varepsilon}\rho\varepsilon) \tag{5}$$

the turbulent viscosity, $\mu_t=\rho C_\mu k^2/\varepsilon$, the production of turbulence kinetic energy k, G_k is computed from $G_k=\mu_t\left(\nabla\vec{v}+(\nabla\vec{v})^T\right):\nabla\vec{v}$. The model constants $C_{1\varepsilon}$, $C_{2\varepsilon}$, C_μ, σ_k and σ_ε have the default values, such as 1.44, 1.92, 0.09, 1.0 and 1.3, respectively. In FLUENT6.2, also in [29], the vapour transport equation is written as

$$\frac{\partial}{\partial t}(\rho f_v)+\nabla\cdot(\rho\vec{v}f_v)=\begin{cases}R_e & p\le p_v\\ -R_c & p>p_v\end{cases} \tag{6}$$

where f_v is the vapour volume fraction in terms of vapour density, $f_v = \alpha_v \rho_v / \rho$; R_e and R_c are the vapour generation and condensation rates expressed as the following

$$\begin{cases} R_e = \frac{0.02\sqrt{k}}{\sigma} \rho_l \rho_v \sqrt{\frac{2(p_v - p)}{3\rho_l}} (1 - f_v - f_g) & p < p_v \\ R_c = \frac{0.01\sqrt{k}}{\sigma} \rho_l \rho_v \sqrt{\frac{2(p - p_v)}{3\rho_l}} f_v & p > p_v \end{cases} \tag{7}$$

where σ is the liquid surface tension, p_v is the modified vapour saturation pressure, $p_v = (p_{\text{sat}} + 0.39\rho k)/2$, p_{sat} is the vapour saturation pressure.

For complex cavitating flows, the standard and linear pressure discretization schemes are not very effective and a second order scheme is desirable. Hence, the governing equations are discretized by using the finite volume method with the staggered-mesh algorithm. The coupling of the continuity equation and momentum equations is accomplished by the SIMPLE algorithm. The second order upwind scheme is implemented in the convection items in the momentum, k and ε equations; in the same kind of item in the vapour transport equation, however, the first order upwind scheme is applied. The second order central difference scheme is kept used in the diffusion items in all the equations. The under relaxation factors are set to be 0.3, 0.5, 0.2, 0.8 and 0.8 for the continuity, momentum, vapour transport, k and ε equations, respectively. The $1 \cdot 10^{-4}$ tolerance is prescribed to terminate the iteration for solving the continuity, momentum, k and ε equations. However, the tolerance for the vapour transport equation is $1 \cdot 10^{-3}$. At the suction pipe entrance, the inlet velocity is enforced and subject to one axial velocity component only, which can be determined by a prescribed flow rate and the known inner cross- section area of the suction pipe. The reference pressure is given to be zero. The pressure-outlet boundary condition remains at the pump discharge nozzle where constant, an as high as 800 kPa, pressure is imposed. The fluid pressure at the impeller entrance is lowered gradually by altering that constant pressure to achieve incipient, slight and serious cavitation. Mesh interfaces are generated in the boundary of the suction pipe outlet and the impeller entrance and in that between the impeller outlet and the vaneless diffuser entrance, respectively. Meanwhile, the wetted shroud and hub of the impeller and vaneless diffuser as well as the inner wall of the suction pipe are subject to the no-slip condition. The rotational periodic boundary condition is imposed in the rest boundary.

3. Results and Discussion

3.1. Head and Hydraulic Efficiency in Non-Cavitating Condition

The head-flow rate curves predicted with three sizes of mesh are delineated in Figure 2 (a) under the non-cavitating condition (single phase flow), the experimental data made in [5, 6] are also presented for comparison. In Figure 2 (b), the pump hydraulic efficiency-flow rate curves are illustrated, moreover a fitting curve for the data under mesh1 is shown concomitantly. The hydraulic loss coefficients in the impeller and the vaneless diffuser plotted as a function of the

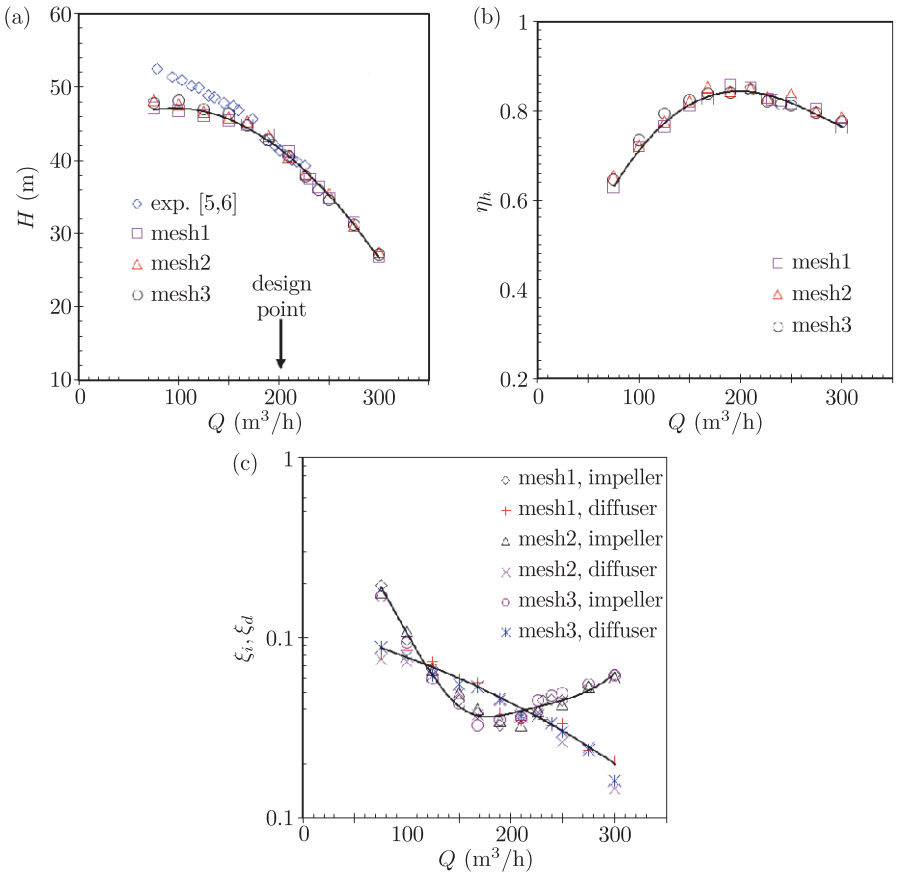

Figure 2. Pump head, hydraulic efficiency and hydraulic loss coefficients across impeller and diffuser plotted as a function of flow rate at three sizes of mesh, the solid line is the fitting curve of data under mesh1, (a) head, (b) hydraulic efficiency, (c) loss coefficient

flow rate are shown in Figure 2 (c), where the loss coefficient in the impeller is defined as $\xi_i = gh_i/u_2^2$, where g is the acceleration due to gravity, $g = 9.81\,\mathrm{m/s^2}$, h_i is the hydraulic loss across the impeller, u_2 is the impeller tip speed; likewise, the loss coefficient in the vaneless diffuser is defined as $\xi_v = gh_v/u_2^2$, h_v is the hydraulic loss across the diffuser. It is shown that the maximum difference in the head and hydraulic efficiency among various sizes of mesh is only 3 %. The predicted head shows good agreement with the observations as the flow rate is higher than $150\,\mathrm{m^3/h}$; unfortunately, the predicted head starts to show a distinct difference from the experimental data as the flow rate falls below $150\,\mathrm{m^3/h}$. The predicted head exhibits a hook shape, the head reaches a maximum at a flow rate of $100\,\mathrm{m^3/h}$.

The hydraulic loss coefficient curve of the impeller is concave up, a minimum coefficient arrives at a flow rate of $175\,\mathrm{m^3/h}$; at both sides of this flow rate, the coefficient increases remarkably, especially for the flow rate lower than $100\,\mathrm{m^3/h}$.

The hydraulic loss coefficient of the diffuser increases with the decreasing flow rate. When the flow rate is in the range of $100\,m^3/h - 220\,m^3/h$, the coefficient of the impeller is less or equal to that of the diffuser; beyond that range, however, the loss coefficient of the impeller is above that of the diffuser, especially when the flow rate is below $100\,m^3/h$.

It is demonstrated that there is a significant deviation in the head predicted from the experimental value when the flow rate is lower than $150\,m^3/h$. This is due to the increasing hydraulic loss in the pump, especially in the impeller. In Figure 2 (c), it is observed that the hydraulic loss coefficient in the vaneless diffuser raises steadily but the coefficient in the impeller increases very rapidly as that flow rate is less than $150\,m^3/h$. To demonstrate this effect even more clearly, the static and kinetic heads of the pump, H_p , H_V and hydraulic loss, $h_i + h_V$, are plotted in Figure 3. It is seen that the hydraulic loss grows very quickly with the decreasing flow rate when the flow rate is lower than $150\,m^3/h$. Also, the static and kinetic heads have a peak value at the flow rate of $100\,m^3/h$. When the flow rate is below this value, the hydraulic loss increases even quicker.

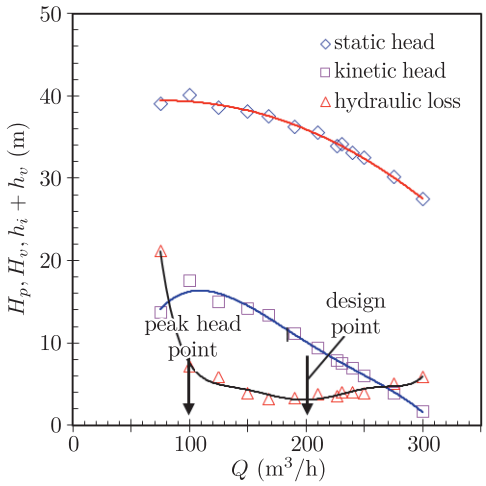

Figure 3. Static and kinetic heads and hydraulic loss in pump against flow rate

The path lines of fluid particles at the flow rate of $100\,m^3/h$ and $75\,m^3/h$ are illustrated in Figure 4. It is confirmed that there is no flow separation in the impeller and diffuser at $100\,m^3/h$ at all. However, the flow separates from the suction side of the blade and the flow in the diffuser is completely stalled at $75\,m^3/h$. a flow separation occurring at the suction side of the blade in a centrifugal pump impeller has been visualized at a part-load point by the well-known experiment in [37]. In the following sections, the full cavitation two phase flow model will be applied to estimate the head of the pump under various NPSHa at the flow rates $168\,m^3/h$, $210\,m^3/h$ and $226.8\,m^3/h$, respectively, and then incipient cavitation number and NPSHr at 3 % head depression will be obtained accordingly.

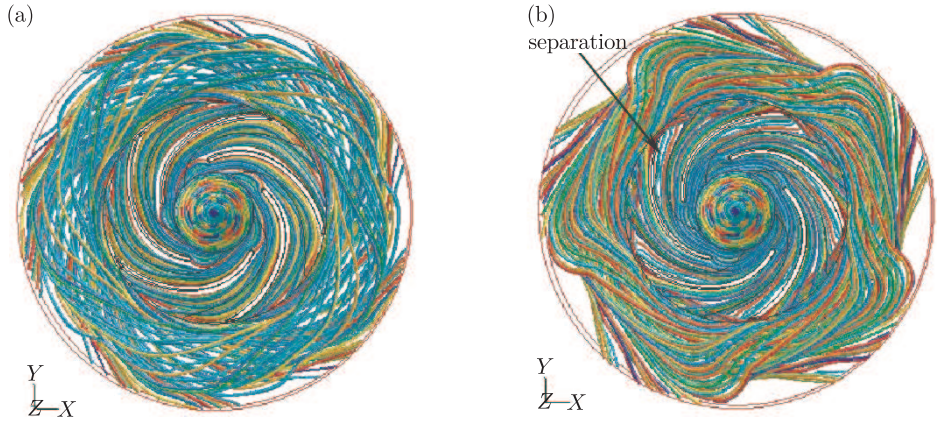

Figure 4. Path line of fluid particles in impeller and vaneless diffuser at two flow rates, (a) 100 m^3/h, (b) 75 m^3/h

In fact, 168 m^3/h, 210 m^3/h and 226.8 m^3/h are three representative flow rates in NPSHr measurements to cover part-load, design and over-load conditions in [5, 6]. Further, the NPSHr at two even low flow rates 120 m^3/h and 100 m^3/h were measured in [6], too. It was turned out that FLUENT was able to predict incipient cavitation numbers at 120 m^3/h and 100 m^3/h, but failed to achieve the NPSHr because of the solution divergence caused by the instability of FLUENT at decreased NPSHa. Therefore, it is only the NPSHr predicted by CFD that will be compared with the experimental data at the flow rates of 168 m^3/h, 210 m^3/h and 226.8 m^3/h.

3.2. Incipient Cavitation

The incipient caviation number was predicted by employing the single phase flow model and the full cavitation two phase flow model under three sizes of mesh and plotted in terms of the flow rate in Figure 5, in which Figure 5 (a) shows the single phase flow model, whereas Figure 5 (b) presents the full cavitation model. Additionally, the incipient cavitation number determined by the cavity visualization that was conducted in [5, 6] is involved in the figure. For the single phase flow model, the incipient cavitation number is defined as $K_i = 2(p_{t1} - p_{\min})/\rho W_1^2$, p_{t1} is the fluid total pressure at the impeller entrance, $p_{\min}$ is the minimum fluid static pressure on the shroud of the impeller or on the surfaces of the blade, W_1 is the fluid relative velocity at the blade leading edge. For the cavitation experiment and two phase flow cavitation model, however, the incipient cavitation number is defined by $K_i = 2(p_{t1} - p_v)/\rho W_1^2$. It is adopted that when cavitation nuclei grow into a bubble cloud with 1 ml volume, the incipient cavitation occurs in the impeller. This value was proposed in [19, 20]. In Figure 5 (a), it is noticed that good agreement in the incipient cavitation number is achieved between prediction and observation when the flow rate is higher than 185 m^3/h for the single phase flow model. In that case, the effect of the mesh size seems less dominant, as well. Unfortunately, as the flow rate is lower than

185 m^3/h, the single phase flow model fails to produce results consistent with observation, and the mesh size appears to illustrate significant influence on the incipient cavitation number. In Figure 2 (a), the predicted head is lower than the measurement as the flow rate is below 185 m^3/h. This suggests that the single phase flow model is challenged and subject to be updated to precisely predict the non-cavitating flow in a centrifugal pump at a low flow rate. In Figure 5 (b), the incipient cavitation number estimated by the full cavitation two-phase flow model agrees well with the observation. This suggests that the model is capable of predicting the occurrence of incipient cavitation with good accuracy.

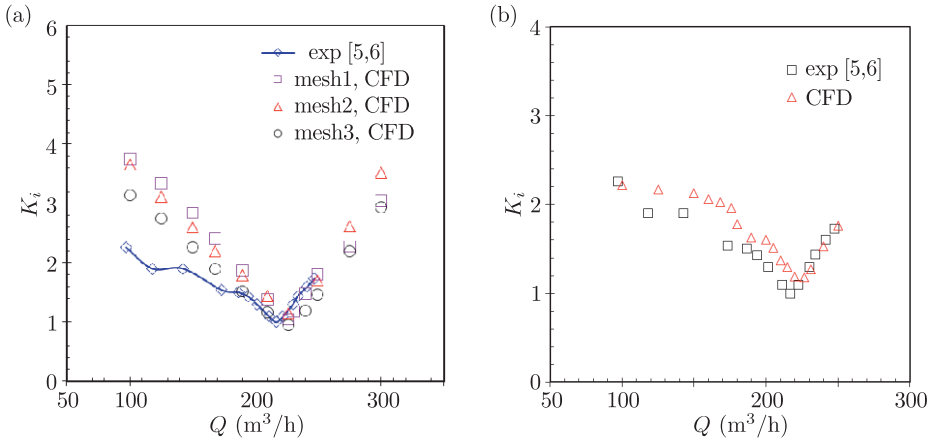

Figure 5. Incipient cavitation number in terms of flow rate, (a) results of single phase flow model against observation, (b) cavitation number of full cavitation model against experimental data

4. Head-NPSHa Curve

The predicted pump head-NPSHa curves are illustrated in Figure 6 under three sizes of mesh at a flow rate of 226.8 m^3/h. It is clear that the curves under different sizes of mesh are consistent with each other. With the decreasing size of mesh, the computational process somehow begins to become unstable at a slightly higher NPSHa, causing eventually a diverged solution at a lower NPSHa. As the head, hydraulic efficiency and head-NPSHa curve estimated under mesh1 were in good agreement with those under the other meshes, it is only the results under mesh1 that are presented in the following sections.

The predicted head-NPSHa curves at three flow rates are compared with the experimental data provided in [5, 6] in Figure 7. Clearly, the estimated NPSHa where the pump head starts to decline is higher than the experimental observation at the same flow rate, moreover, the predicted head drops more quickly against NPSHa than the experimental one. This indicates that the default setting of the parameters in the full cavitation model in FLUENT cannot generate quite good results for the experimental pump [5, 6].

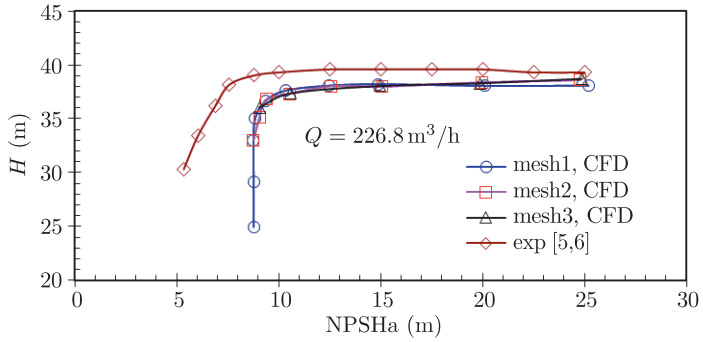

Figure 6. Relationship between pump head and NPSHa under three numbers of cells of mesh

The predicted, experimental NPSHr and blade cavitation coefficients are tabulated in Table 3 to identify the difference between CFD prediction and experiment at three flow rates. The ratio of experimental NPSHr over CFD NPSHr, and the experimental blade cavitation coefficient over the CFD blade cavitation coefficient are presented, too. It should be noted that those ratios depend on the flow rate, namely the higher the flow rate, the greater the ratio; this means that an estimated NPSHr approaches the experimental one more closely with the increasing flow rate. The blade cavitation coefficient λ accounts for the dynamic pressure depression of fluid when it flows around the blade leading edge profile, and is involved in the following NPSHr equation of a centrifugal pump in an impeller [1, 38]

$$\text{NPSHr} = \lambda_1 \frac{V_1^2}{2g} + \lambda \frac{W_1^2}{2g} \tag{8}$$

where λ_1 is the empirical coefficient accounting for entry loss in the suction chamber and non-uniform velocity at the impeller entrance, $\lambda_1 = 1.2$, V_1 is the fluid absolute velocity at the blade leading edge, W_1 is the relative velocity of fluid at the blade leading edge, $W_1 = \sqrt{V_1^2 + u_1^2}$ for the case without pre-swirl, u_1 is the tip speed of the blade leading edge, $u_1 = \pi n d_1/60$, d_1 is the diameter of the blade leading edge.

Substituting the CFD predicted NPSHr or experimental $\text{NPSHr}^{\text{exp}}$ into (8), and then the theoretical cavitation coefficient λ or experimental cavitation coefficient λ^{exp} can be determined by

$$\lambda = \frac{2g\text{NPSHr} - \lambda_1 V_1^2}{W_1^2} \tag{9}$$

The ratio of vapour plus non-condensable gas volume V_C over liquid volume V_L in the impeller is plotted in terms of NPSHa in Figure 8 (a), and the head against V_C/V_L is plotted in Figure 8 (b) at three flow rates. The ratio V_C/V_L remains rising with the decreasing NPSHa, meanwhile the head keeps being degraded. It is clear that the moment of V_C/V_L rapid increase is the instant when the head is subject to a remarkable decrease. This indicates that the head distortion is ascribable to the occurrence of vapour in the impeller. Figure 8 (b) seems to imply

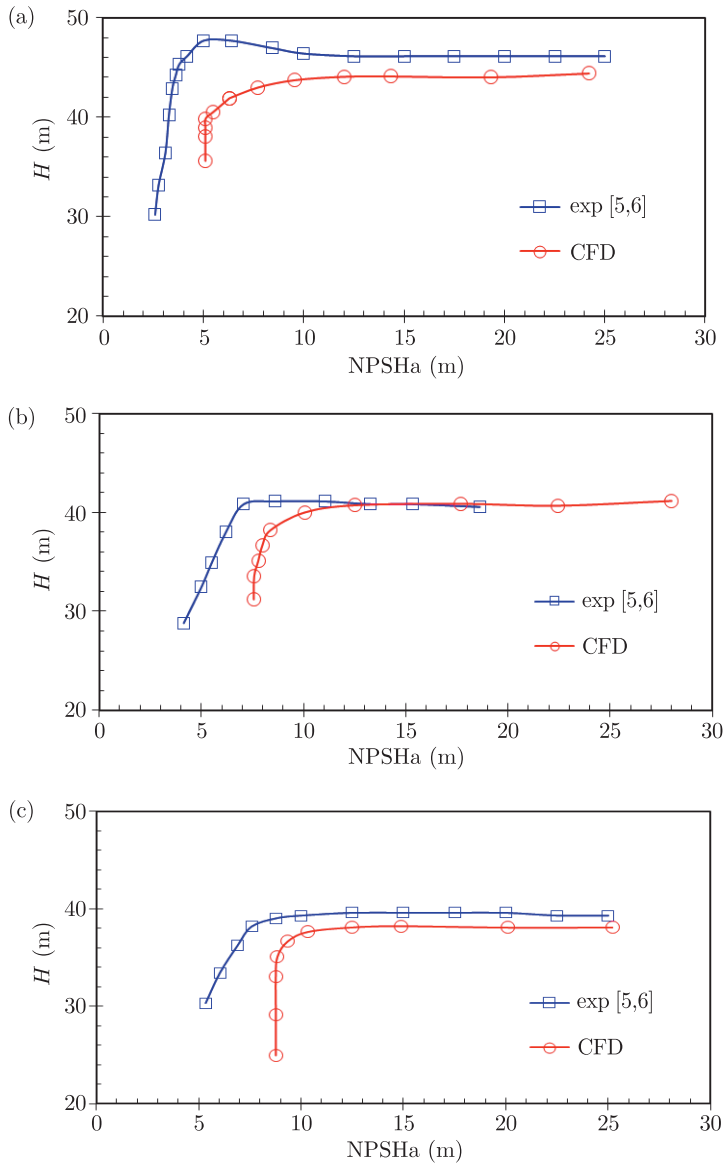

Figure 7. Pump head shown in terms of NPSHa at three flow rates, (a) $Q = 168\,\mathrm{m}^3/\mathrm{h}$, (b) $Q = 210\,\mathrm{m}^3/\mathrm{h}$, (c) $Q = 226.8\,\mathrm{m}^3/\mathrm{h}$

Table 3. Predicted NPSHr, blade cavitation coefficient and those measured in [5, 6]

Q (m^3/h)	$\mathrm{NPSHr}^{\mathrm{exp}}$ (m)	NPSHr (m)	$\mathrm{NPSHr}^{\mathrm{exp}}/\mathrm{NPSHr}$	λ^{exp}	λ	$\lambda^{\mathrm{exp}}/\lambda$
168	5.29	7.32	0.7227	0.2915	0.4550	0.6405
210	6.61	8.36	0.7907	0.3029	0.4355	0.6955
226.8	7.90	9.20	0.8587	0.3579	0.4537	0.7887
Mean $\mathrm{NPSHr}^{\mathrm{exp}}/\mathrm{NPSHr}$			0.7907	Mean $\lambda^{\mathrm{exp}}/\lambda$		0.7082

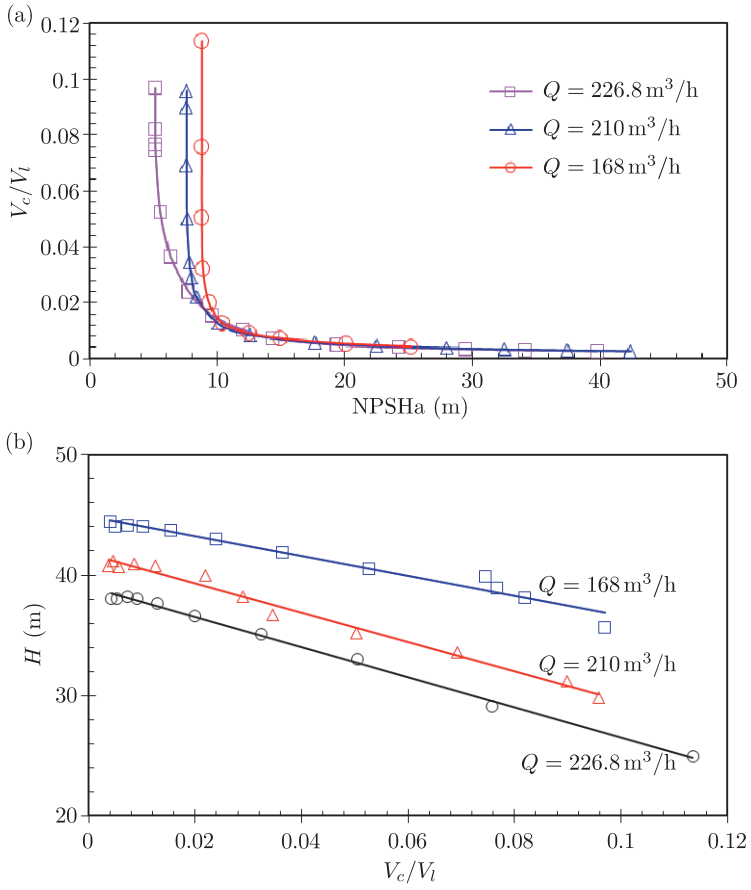

Figure 8. Vapour-liquid volume ratio against NPSHa and head versus vapour-liquid volume ratio, (a) vapour-liquid volume ratio against NPSHa, (b) head against vapour-liquid volume ratio

that the pump head can be correlated to the integrated vapour-liquid volume ratio V_C/V_L in the impeller. To confirm this, the scattered data of the head and integrated vapour-liquid volume ratio are fitted with a linear equation; the results are presented in (10). It is evident that there is a linear relationship between the two parameters.

$$\begin{cases} H = -80.704(V_c/V_L) + 44.737 & R^2 = 0.966 & Q = 168\,\mathrm{m}^3/\mathrm{h} \\ H = -122.810(V_c/V_L) + 41.799 & R^2 = 0.986 & Q = 210\,\mathrm{m}^3/\mathrm{h} \\ H = -124.680(V_c/V_L) + 39.010 & R^2 = 0.997 & Q = 226.8\,\mathrm{m}^3/\mathrm{h} \end{cases} \tag{10}$$

where R is the correlation coefficient in the context of linear regression. Moreover, the negative slope decreases with the increasing flow rate, see (10), i.e. the rate of decline in the head against the integrated vapour-liquid volume ratio decreases with the increasing flow rate. This means that the head becomes more and more sensitive to the integrated vapour-liquid volume ratio with the increasing flow rate.

4.1. Effects of Non-Condensable Gas Content and Turbulence Model

The head-flow rate curve was also estimated using the RNG k-ε turbulence model. At the same time, a series of unsteady flow simulations were launched as well based on the standard k-ε turbulence model. The corresponding head curves are shown in Figure 9. The RNG k-ε model results in even poor prediction compared with the observation. The head curve of unsteady simulation is in good agreement with that of the steady flow. Those facts seem to suggest that the flow model used exaggerated the hydraulic loss in the pump at an off-design condition.

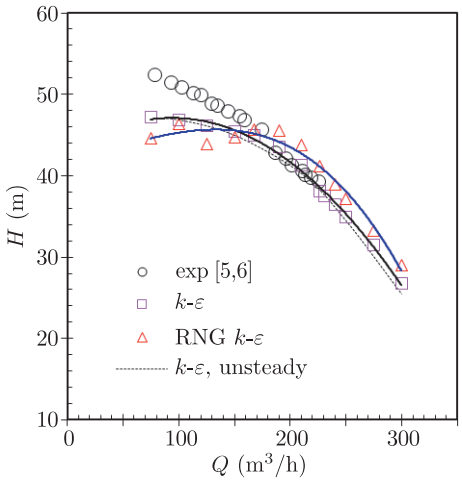

Figure 9. Non-cavitating head-flow rate curves predicted by using steady flow model based on the standard and RNG k-ε turbulence model and those estimated by means of unsteady flow model and the standard k-ε model

The influence of the non-condensable gas content and the turbulence model on the head- NPSHa curve is shown in Figure 10. It can be seen from Figure 10 (a) that it is only when the non- condensable content is higher than 15 ppm that it starts to alter the head-NPSHa curve, i.e. to arise the NPSHr. Otherwise, the head-NPSHa curve or NPSHr is little affected by the non-condensable gas content.

In Figure 10 (b), the RNG k-ε turbulence model not only increases the pump head but raises the NPSHr level, as well. It is very bad that the model allows the computational process to be unstable, eventually resulting in a divergence with decreasing NPSHa. To this end, the head breakdown condition arising from severe cavitation cannot be achieved with this model. The NPSHr predicted with the RNG k-ε turbulence model is as high as 10.7 m comparing with the 7.9 m experimental value and the 9.2 m estimate by using the standard k-ε turbulence model. This suggests that the RNG k-ε turbulence model has poor performance in the NPSHr prediction. In Figure 11, the incipient cavitation number is plotted against the flow rate based on the RNG k-ε turbulence model. Even though

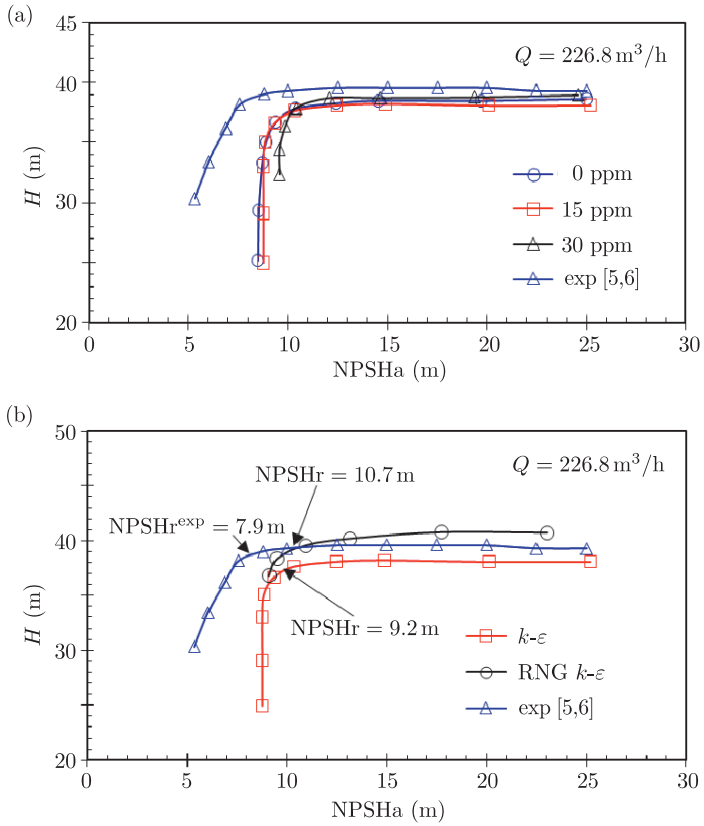

Figure 10. Effects of non-condensable gas content and turbulence model on head-NPSHa curve, (a) non-condensable gas content, (b) turbulence model, the arrows indicate the positions of 3 % head drop

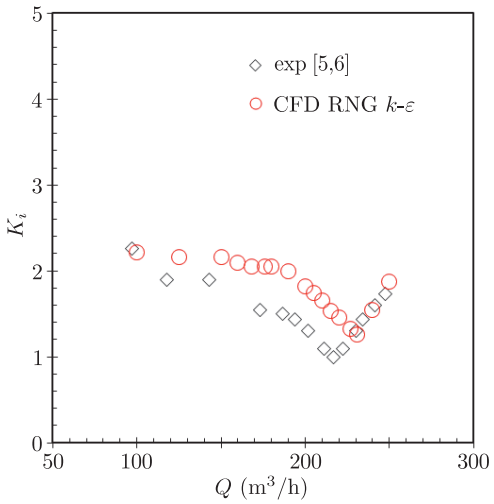

Figure 11. Incipient cavitation number in terms of flow rate based on RNG k-ε turbulence model

the predicted incipient cavitation number curve is in good agreement with the observation in [5, 6] at a high flow rate, it still exhibits a remarkable difference from that observation at a low flow rate. Comparing with Figure 5 (b), the RNG k-ε turbulence model shows poor capacity for predicting the incipient cavitation in a centrifugal pump impeller.

4.2. Cavitation Expansion within the Impeller

The predicted and experimental cavity patterns in the impeller are illustrated in Figure 12 at 3 % pump head depression. At a low flow rate (part-load condition, $Q = 168\,\mathrm{m}^3/\mathrm{h}$), the cavity is mainly located at the blade suction side as the blade is subject to a positive angle of attack. However, under the design condition ($Q = 210\,\mathrm{m}^3/\mathrm{h}$), the cavity emerges on the blade suction side and shroud simultaneously; clearly, the experimental cavity locations are in good agreement with the CFD prediction. At a high flow rate (over-load condition, $Q = 226.8\,\mathrm{m}^3/\mathrm{h}$), the cavity that is on the blade suction side at the low flow rate disappears, but it appears on the blade pressure side since the blade is under a negative angle of attack. The other cavity remains on the shroud with the highest vapour volume fraction.

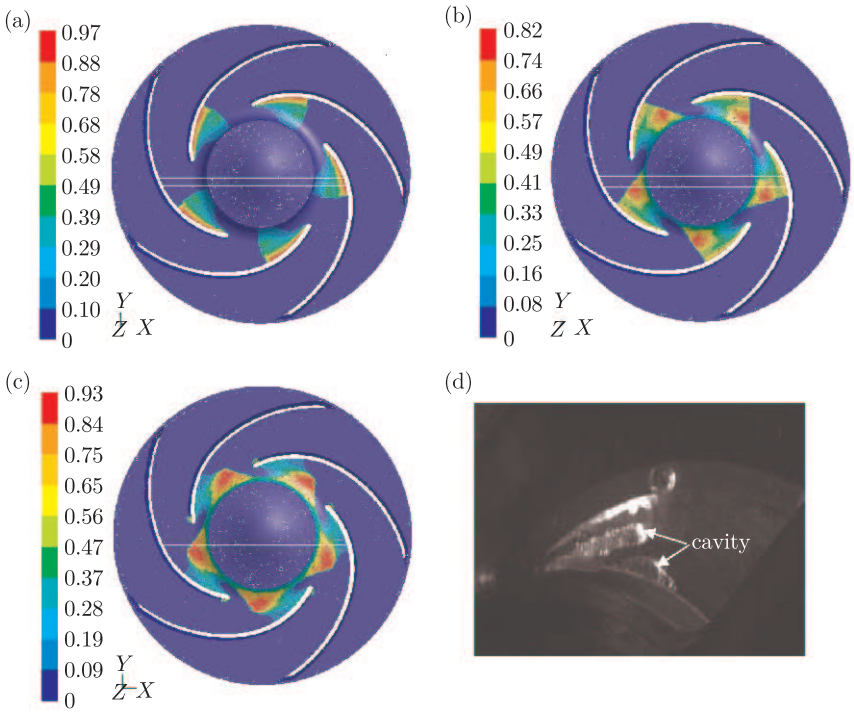

Figure 12. Cavity patterns in the impeller under part-load, design and over-load conditions at 3 % pump head drop, (a) part-load, $Q = 168\,\mathrm{m}^3/\mathrm{h}$, CFD, (b) design, $Q = 210\,\mathrm{m}^3/\mathrm{h}$, CFD, (c) over-load, $Q = 226.8\,\mathrm{m}^3/\mathrm{h}$, CFD, (d) design, $Q = 210\,\mathrm{m}^3/\mathrm{h}$, experimental observation in [5], the legend indicates the vapour volume fraction scale

4.3. Discussion

In light of Figure 5, the full cavitation two phase flow model can predict the incipient cavitation number reasonably at all flow rates. The single phase viscous fluid flow model can estimate the number quite well under the design and over-load conditions as well; it requires much less computing time compared with the two phase flow model. Therefore, in incipient cavitation performance optimization of a centrifugal pump it is a reasonable to choose a single phase flow model since substantial computational time can be saved.

The incipient cavitation performance of a centrifugal pump under design and over-load conditions can be even predicted by using the potential flow model [32, 33] or the viscid single flow model [23] or (8) where the blade cavitation coefficient λ is a function angle of attack [39] or the coefficient is related to more parameters such as the impeller meridional profile, blade-load, Coriolis effect, blade angle and width gradient along streamline, blade thickness blockage and angle of attack based on the well-known quasi three- dimensional inviscid flow model [40].

If NPSHr were to be optimized (reduced), a two phase flow cavitation model should be utilized because a pump impeller with the lowest incipient cavitation performance does not mean to have the lowest NPSHr, either. The relationship between the incipient cavitation number and NPSHr is non-linear and quite complicated [41].

It should be noted that the incipient cavitation criterion adopted here differs from that proposed in [34] where the cavitation inception was denoted by growth to 1.3 mm for a nucleus bubble. The full cavitation model is Eulerian method-based, thus, the bubble size criterion is inapplicable for the model. In [9], cavitation inception is defined as the state of $p = p_v$ on the blade surfaces in the mass transfer model shown by (7). Unfortunately, this criterion results in under-predicted incipient cavitation numbers. Since a cavitating process can be affected by many factors, namely, the type of liquid, temperature pumped, viscosity, impurity, non-condensable gas concentration, pipe cleanliness, bubble filtering method and pipe valves, etc, one pump may exhibit a slightly different head-NPSHa curve in different experimental rigs [42], therefore it is unrealistic to request a cavitation model applicable for all cases.

In Figure 7, the head-NPSHa predicted by the full cavitation model is quite different in shape and value of NPSHr. The reasons for this may be the following: (1) the cavitating process is highly dependent of water quality, i.e. tension strength [43–45]; however, there is no information about the water quality or tension strength in [5, 6]. Besides, the full cavitation model does not seem to consider the effect related to the water quality. (2) Clearly, the shape of the head drop against NPSHa in the experiment is a considerable difference from that in the CFD outcome, this means that the predicted head shows a very sharp drop in terms of NPSHa. This may be caused by the simplified condition in the cavitation model, where the second-order and nonlinear first-order of the bubble

radius change rate with time in the bubble growth and collapse equation in [29] have been omitted. (3) There are several empirical model parameters in the full cavitation. They were validated with limited cavitating flow cases, obviously the determined parameters are unlikely applicable to every case. In the paper, we do not tend to alter the parameters for fitting the experimental data, but just to predict the cavitation performance with the default setting and to check the difference between observation and estimation.

The forthcoming work includes the full cavitation model validation when a centrifugal pump is under the condition of pumping viscous oils and the viscous oil-based two-phase flow cavitation model development.

5. Conclusions

In the paper, the incipient cavitation behaviour and cavitation performance were investigated by means of the CFD code and the full cavitation model for the experimental centrifugal pump with a vaneless diffuser in [5, 6] when handling water. The predicted incipient cavitation number and NPSHr were compared with the experimental results. Besides, the effects of the non-condensable gas concentration and the turbulence model on the head-NPSHa curve were explored, and a relation between the pump head and the integrated vapour-liquid volume ratio was established. The full cavitation model is capable of predicting the incipient cavitation behaviour of the pump with a better accuracy. Meanwhile, at design and high flow rates, the single phase viscid flow model can produce a fairly accurate incipient cavitation number. The error in the NPSHr between the full cavitation model prediction and the experimental value is dependent on the flow rate. There is a linear relationship between the pump head and the integrated vapour-liquid volume ratio in the impeller, the head becomes more and more sensitive to the integrated vapour-liquid volume ratio with the increasing flow rate. The non-condensable gas is unable to give rise to an effect upon the head-NPSHa curve and the NPSHr until its content is higher than 15 ppm. Compared with the standard k-ε turbulence model, the RNG k-ε turbulence model results in an increased pump head rise, and shows instability during the computational process, eventually the cavitation breakdown condition is not reachable. The predicted cavity in the impeller is consistent with the visualized one under the design conditions.

Acknowledgements

The author would like to thank Professor Bernd Stoffel at Technische Universität Darmstadt, Germany, who kindly offered a permission to use two figures in [5, 6] as Figure 1 (a) and (b), Figure 12 (d) herein.

References

[1] Minami S and Kawaguchi K 1960 *Bulletin of JSME* **3** (9) 19
[2] Yokoyama S 1960 *Bulletin of JSME* **3** (11) 326
[3] Kasai T and Takamatu Y 1963 *Transitions of the JSME, Series 2* **29** (204) 1308
[4] Kasai T, Takamatu Y 1964 *Bulletin of JSME* **7** (27) 543

[5] Hofmann M, Stoffel B, Coutier-delgosha O, Fortes-Patella R and Reboud J L 2001 *Experimental and numerical studies on a centrifugal pump with 2D-curved blades in cavitating condition*, Proceedings of the 4th International Symposium on Cavitation, California Institute of Technology, Pasadena, California, USA
[6] Hofmann M, Stoffel B, Friedichs J and Kosyna G 2001 *Similarities and geometrical effects on rotating cavitation in two scalded centrifugal pumps*, Proceedings of the 4th International Symposium on Cavitation, California Institute of Technology, Pasadena, California, USA
[7] Hirschi R, Dupont P, Avellan F, Favre J N, Guelich J F and Parkinson E 1998 *ASME Journal of Fluids Engineering* **120** (4) 705
[8] Wursthorn S and Schnerr G H 2001 *ZAMM* **81** 579
[9] Medvitz R B, Kunz R K, Boger D A, Lindau J W, Yocum A M and Pauley L L 2002 *ASME Journal of Fluids Engineering* **124** (2) 377
[10] Athavale M M, Li H Y, Jiang Y and Singhal A 2002 *International Journal of Rotating Machinery* **8** (1) 45
[11] Couier-Delgosha O, Patella R R, Rebound J L, Hofmann M and Stoffel B 2003 *ASME Journal of Fluids Engineering* **125** (6) 970
[12] Dupont P and Okamura T 2003 *International Journal of Rotating Machinery* **9** (3) 163
[13] Nohmi M, Goto A, Iga Y and Ikohagi T 2003 *Cavitation CFD in a centrifugal pump*, Proceedings of the 5th International Symposium on Cavitation, Osaka, Japan
[14] Luo X W, Nishi M, Yoshida K, Dohzono H and Miura K 2003 *Cavitation performance of a centrifugal impeller suitable for mini turbo-pump*, Proceedings of the 5th International Symposium on Cavitation, Osaka, Japan
[15] Dupont P 2004 *Numerical prediction of cavitation in pumps*, Proceedings of the 18th International Pump Users Symposium, Turbomachinery Laboratory, Texas A&M University, USA 59
[16] Li J, Liu L J and Feng Z P 2006, Proceedings of the Institution of Mechanical Engineers, Part A: Journal of Power and Energy, 220 783
[17] Pouffary B, Patella R F, Rebound J L and Lambert R A 2008 *ASME Journal of Fluids Engineering* **130** (6), 061301–1-10
[18] Pierrat D, Gros L, Pintrand G, Le Fur B and Gyomlai Ph 2009 *Experimental and numerical investigations of leading edge cavitation in a helicon-centrifugal pump*, Proceedings of the 12th International Symposium on Transport Phenomena and Dynamics of Rotating Machinery, Honolulu, Hawii, USA 1
[19] Stuparu A, Muntean S, Susan-Resiga R, and Anton L 2009 *Numerical investigation of the cavitational behavior of a storage pump*, Proceedings of the 3rd IAHR International Meeting of the Workgroup on Cavitation and Dynamic Problems in Hydraulic Machinery and Systems, Brno, Czech Republic
[20] Stuparu A, Susan-Resiga R, Anton L and Muntean S 2011 *International Journal of Fluid Machinery and Systems* **4** (1) 104
[21] Balasubramanian R, Sabini E and Bradshaw S 2011 *Influence of impeller leading edge profile on cavitation and suction performance*, Proceedings of the 27th International Pump Users Symposium, Turbomachinery Laboratory, Texas A&M University, Houston, Texas, USA 34
[22] Zhuang B T, Luo X W, Zhu L, Wang X and Xu H Y 2011 *International Journal of Fluid Machinery and Systems* **4** (1) 191
[23] Ding H, Vissr F C, Jiang Y and Furmanczyk M 2011 *ASME Journal of Fluids Engineering* **133** (1), 0110101-1-14
[24] Hedi L, Hatem K and Ridha Z 2012 *Science of Academy Transactions on Renewable Energy Systems Engineering and Technology* **2** (1) 179

[25] Somashekar D and Purushothama H R 2012 *IOSR Journal of Mechanical and Civil Engineering* **1** (5) 21
[26] Zwart P, Gerber A G and Belamri T 2004 *A two-phase model for predicting cavitation dynamics*, Proceedings of the 5th International Conference on Multiphase Flow, Yokohama, Japan 1
[27] Schnerr G H and Sauer J 2001 *Physical and numerical modeling of unsteady cavitation dynamics*, Proceedings of the 4th International Conference on Multiphase Flow, New Orleans, USA 1
[28] Kunz R F, Boger D A, Stinebring D R, Chyczewskia T S, Lindaua J W, Gibelinga H J, Venkateswaranb S and Govindanc T R 2000 *Computers and Fluids* **29** (8) 849
[29] Singhal A K, Athavale M M, Li H and Jiang Y 2002 *ASME Journal of Fluids Engineering* **124** (3) 617
[30] Ishihara T 1982 *Transactions of the JSME, Series B* **48** (434) 1829
[31] Li W G 2012 *Pump Technology* **6** 1
[32] van Os M J, op de Woerd J G H and Jonker J B 1997 *A parametric study of the cavitation inception behavior of a mixed-flow pump impeller using a three-dimensional potential flow model*, Proceedings of the ASME Fluids Engineering Division Summer Meeting, Vancouver, Canada
[33] Visser F C, Dijkers R J H and op de Woerd J G H 2000 *Computing Visualization in Science* **3** (1–2) 103
[34] Farrell K 2003 *ASME Journal of Fluids Engineering* **125** (1) 46
[35] Pisarenco M, van der Linden B, Tijsseling A, Ory E and Dam J 2011 *ASME Journal of Offshore Mechanics and Arctic Engineering* **133**, 011101-1-8
[36] Anonymous 2005 *FLUENT 6.2 User's Guide, Volume 1 and 2*, Fluent Inc
[37] Fisher K 1946 *Investigation of flow in a centrifugal pump*, NACA TM-1089
[38] Palgrave R and Cooper P 1987 *Visual studies of cavitation in pumping machinery*, Proceedings of the 3rd International Pump User Symposium, Turbomachinery Laboratory, Texas A&M University, USA 61
[39] Gopalakrishman S 1985 *Modern cavitation criteria for centrifugal pumps*, Proceedings of the 2nd International Pump User Symposium, Turbomachinery Laboratory, Texas A&M University, USA 3
[40] Ardizzon G and Pavesi G 1995 *Theoretical evaluation of the effects of the impeller entrance geometry and of the incidence angle on cavitation inception in centrifugal pumps*, Proceedings of the Institution of Mechanical Engineers, Part C: Journal of Mechanical Engineering Science, 209 29
[41] Wan S Y, Mu J G and Ye B 1990 *An approach to cavitation criterion selection and impeller design methods for centrifugal pumps*, Proceedings of the 3rd Japan-China Joint Conference on Fluid Machinery, Volume I, Osaka, Japan 169
[42] Hirotsu M and Kang C M 1968, Memoirs of the Institute of Sciences and Technology, Meiji University **7** 79
[43] Arndt R E A and Keller A P 1992 *ASME Journal of Fluids Engineering* **114** (3) 430
[44] Eickmann G 1993 *Journal of Hydraulic Research* **31** (3) 347
[45] Keller A P 2001, Proceedings of the 4th International Symposium on Cavitation, California Institute of Technology, Pasadena, CA, USA